

# Self-supervised Representation Learning for Reliable Robotic Monitoring of Fruit Anomalies

Taeyeong Choi<sup>1</sup>, Owen Would<sup>2</sup>, Adrian Salazar-Gomez<sup>1</sup>, and Grzegorz Cielniak<sup>1</sup>

**Abstract**—Data augmentation can be a simple yet powerful tool for autonomous robots to fully utilise available data for self-supervised identification of *atypical* scenes or objects. State-of-the-art augmentation methods arbitrarily embed structural peculiarity in focal objects on typical images so that classifying these artefacts can provide guidance for learning representations for the detection of anomalous visual inputs. In this paper, however, we argue that learning such structure-sensitive representations can be a suboptimal approach to some classes of anomaly (e.g., unhealthy fruits) which are better recognised by a different type of visual element such as “colour”. We thus propose *Channel Randomisation* as a novel data augmentation method for restricting neural network models to learn encoding of “colour irregularity” whilst predicting *channel-randomised* images to ultimately build reliable fruit-monitoring robots identifying atypical fruit qualities. Our experiments show that (1) the colour-based alternative can better learn representations for consistently accurate identification of fruit anomalies in various fruit species, and (2) validation accuracy can be monitored for early stopping of training due to positive correlation between the colour-learning task and fruit anomaly detection. Moreover, the proposed approach is evaluated on a new anomaly dataset *Riseholme-2021*, consisting of 3.5K strawberry images collected from a mobile robot, which we share with the community to encourage active agri-robotics research.

## I. INTRODUCTION

Agricultural mobile robots are expected to precisely assess the qualities of crops from their sensory information to autonomously perform the targeted treatment of individual plants or harvest the mature and healthy crops. To realise this autonomy, deep learning models could be adopted to classify visual input from robotic sensors by optimising their parameters based on a large number of examples available in advance. In practice, however, collecting data of “atypical” qualities, e.g., fruits with disease or damage, can be challenging mainly because of their rare occurrences, and therefore, One-class Classification (OC) paradigm [1], [2] has been widely used in computer vision communities, in which classifiers are trained to maximise the utility of the available data from “normal” class to later distinguish unseen instances of “anomalous” class as well.

Self-supervised Learning (SL) has been introduced as a powerful method to effectively solve OC problems by augmenting training data to inject some level of *unusual* patterns because classifying the artefacts can be an instructive proxy task to learn potentially informative feature representations for detecting anomalies in tests [3], [4], [5], [6]. Nonetheless, most successful SL tasks have been designed only for the

All authors are with the Lincoln Agri-Robotics (LAR) Centre, Lincoln, UK. <sup>1</sup>{tchoi, asalazargomez, gcielniak}@lincoln.ac.uk, <sup>2</sup>25393497@students.lincoln.ac.uk

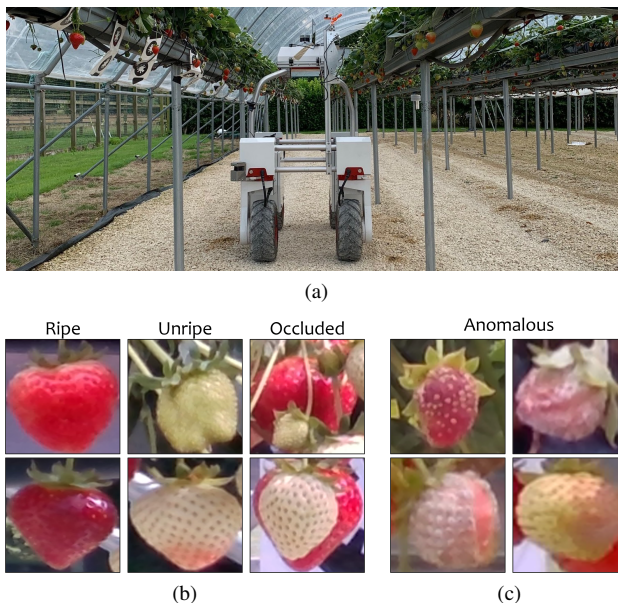


Fig. 1: (a) Robotic monitoring of anomalous strawberries using a mobile sensing platform *Thorvald*; Sample categories from *Riseholme-2021* dataset including (b) three “normal” subcategories and (c) “anomalous”.

scenarios in which anomaly is mostly defined by *structural* differences – e.g., bent tips in screws, holes on hazelnut bodies, or missing wires in cable clusters in MVTec AD Dataset [7] – or image samples out of a particular training class in large datasets such as ImageNet [8] or CIFAR-10 [9].

We argue that such representation learning techniques may only provide suboptimal performance for OC in agricultural domains since anomalies in fruits, for example, tend to appear with only little distinction in shape, but peculiar *pigmentations* (e.g., Fig. 1c) instead could be more useful visual cues for differentiation. As an alternative, in this paper, we thus propose *Channel Randomisation* (CH-Rand), which augments each image of normal fruit by randomly permutating RGB channels with a possibility of repetition so as to produce *unnatural* “colour” compositions in the augmented image. Whilst classifying these artefacts, the neural networks automatically learn discriminative representations of irregular colour patterns, so that distance-based heuristics can later be employed on that learnt space to estimate the anomaly score of normal input using the distance to the existing data points.

To validate the performance of our system in a realistic

scenario, we also introduce *Riseholme-2021*, a new dataset of strawberry images, for which we operated a mobile robot (Fig. 1a) to collect 3,520 images of healthy and unhealthy strawberries at three unique developmental stages with possible occlusions (cf. Fig. 1b-1c). Our experiments show that CH-Rand is the most reliable method for representation learning amongst all other baselines including self-supervised structure-learning methods (e.g., CutPaste [3]) in anomaly detection on our strawberry dataset but also on several other fruits in the publicly available *Fresh & Stale* dataset. We further support our design of SL by demonstrating high degrees of correlation between the success in colour prediction task and the performance in anomaly identification. Hence, CH-Rand does not require manually engineered criteria for early stopping, and validation accuracy can simply be monitored during the proxy task to ensure high-performance anomaly detector.

## II. RELATED WORK

### A. Anomaly Detection in Agricultural Domains

Perception models have played a crucial role also in agriculture to build up essential capabilities to eventually deploy fully autonomous robots in real farms. For instance, weeds are targeted anomalies to detect in [10], [11], [12], and occlusions or dense fruit clusters are of interest in [13], [14]. More relevantly to our work, plant diseases are also important anomalies to detect as in [15], [16], [17], in which networks were trained with annotated images to learn leaves with diseases. These methods were built upon supervised learning aided by manually annotated data, but our approach is designed to meet the practical assumption in OC that anomalous data may be unavailable during training. Hossain et al. [18] also utilised colour-based features to recognise anomalous leaves, but they only depended on human engineered features, while ours trains deep neural networks.

### B. One-class Classification Strategies

Due to the strict assumption in OC, generative model-based frameworks have been widely used. For instance, Deep Convolutional Autoencoders (DCAE) measure the reconstruction error because novel data would more likely cause higher errors [1], [19]. With DCAE as a backbone, Ruff et al. [2] introduced Deep Support Vector Data Description (DSVDD) to learn as dense representations near a central vector  $\vec{c}$  as possible so that atypical data points would be detected by a long distance from it. Generative Adversarial Networks (GANs) can also provide a large benefit by synthesis of data to potentially model unavailable anomalous samples [1], [20], [21], [22]. For example, IO-GEN [1] utilises a trained DSVDD to replace its  $\vec{c}$  with synthetic data to perform multi-dimensional classification for complex datasets in place of simplistic distance calculation.

1) *Self-supervised Learning*: The ultimate goal in SL is to gain useful representations in neural networks for future anomaly detection whilst identifying intentionally manipulated data as a *pretext* task. For example, inferring (1) geometric transformations such as rotation (ROT) applied

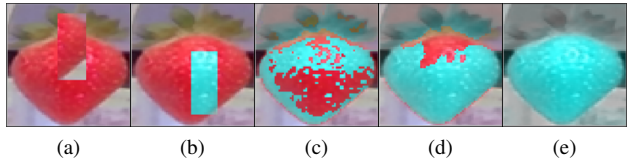


Fig. 2: Various data augmentations on an image of ripe strawberry: (a) CutPaste [3] and “BRR” permutation applied by CH-Rand to (b) a local patch, (c) 50% thresholded pixels, (d) a segment of Sobel filter [28], and (e) all pixels.

to input images [23], (2) relative locations among regional patches [5], or (3) images with blank local masks embedded [4] has shown great successes for OC. More recently, Li et al. [3] introduced CutPaste (CP), in which unlike [4], local patches are extracted directly from the original images (cf., Fig. 2a) to keep the proxy task more challenging.

In fact, all these augmentations were motivated to model typical structures of normal objects (e.g., defect-free screws) to detect odd shapes in anomalous examples (e.g., screws with bent tips) afterwards. We, however, argue that such structural difference may be less significant in differentiation between healthy and unhealthy fruits, and we propose to learn *colour regularity* instead as an alternative.

### C. Channel Randomisation for SL

Although colourisation can be used to learn useful representations by colouring grayscale images [24], [25], a more relevant technique to CH-Rand is *Channel Permutation* (CH-Perm) [26], also called *Channel Swap* [27], in which six possible random permutations are considered to shuffle image channels. *Channel Splitting* (CH-Split) [27] is also related, in which a randomly chosen representative channel is applied to all others. Lee et al. [27] applied this to their SL framework to encourage their models to “ignore” colour variations but learn semantic coherence through a human action. In contrast, we adopt CH-Rand to “consider” colour patterns in representation learning. Also, CH-Rand can generate a larger set of 27 channel sequences including the ones that CH-Perm and CH-Split can generate, so in Section IV, we investigate the benefits from using it.

## III. METHODOLOGY

As in previous approaches [3], our framework includes two modular processes for anomaly identification on fruit images: (1) self-supervised representation learning with data augmentation and (2) anomaly score estimation. In III-A, we first formalise our proposed CH-Rand augmentation and then in III-B, describe a heuristic method to calculate anomaly scores on learnt representations.

### A. Channel Randomisation

Our approach is motivated by the unique observations of fruit anomalies compared to other types – i.e., local defects on industrial products in MVTEC AD [7] or the out-of-distribution samples in CIFAR-10 [9]. To be specific,

as shown in Fig. 1b, fruits generally have relatively high phenotypic variations in local structures even in the same species regardless of normality; nevertheless, healthy fruits at the same developmental stage all share a similar colour composition which can change dramatically as the fruit becomes unhealthy, for example due to some fungal infection as displayed in Fig. 1c. Therefore, we design a novel augmentation method to restrict the neural network to learn representations for encoding *colour irregularity* to ultimately build a more reliable anomaly detector on agricultural robots.

CH-Rand can be simply performed by computing a random permutation of colour channels with a possibility of repetition to apply to the entire image input. More formally, we generate an augmented image  $\mathcal{A} \in \mathbb{R}^{W \times H \times C}$  by executing CH-Rand on the original image  $\mathcal{I} \in \mathbb{R}^{W \times H \times C}$  of normal class available during training, where  $W$  and  $H$  are the width and the height, respectively, and  $C$  is the number of channels, which is typically set to 3 for the RGB image format. To augment a new input  $\mathcal{I}$ , we first randomly build an arbitrary permutation function  $\pi : \chi \rightarrow \chi'$ , where  $\chi = \{1, 2, \dots, C\}$ , and  $\chi' \in \mathcal{P}(\chi) \setminus \emptyset$  as  $\mathcal{P}$  returns the powerset of input. Note that the output *sequence* by  $\pi$  may have some repetition by design because  $|\chi'| \leq |\chi|$ . Moreover, we keep drawing a new  $\pi$  until  $\exists c \in \chi, c \neq \pi(c)$  to avoid the case of  $\mathcal{A} = \mathcal{I}$ . As a result, 26 possible channel sequences exist for augmentation in 3-channel format, whereas Ch-Split and Ch-Perm only have three and six possibilities, respectively.

Each element  $a_{w,h}^c$  in  $\mathcal{A}$  can then be determined as follows:

$$a_{w,h}^c = i_{w,h}^{\pi(c)}, \quad (1)$$

for which  $\pi$  is fixed for all  $w, h$ , and  $c$ . An example with BBR colour channel permutation is presented in Fig. 2e.

Based upon this augmentation method, a classifier can be set to learn the binary classification to predict whether input images are the products of the augmentations. Inspired by [3], [23], we design our loss function below to train a deep neural network-based classifier  $f_\Theta$  on a training dataset  $\mathcal{D}$ :

$$\mathcal{L} = \mathbb{E}_{\mathcal{I} \in \mathcal{D}} [H(f_\Theta(\mathcal{I}), 0) + H(f_\Theta(\text{CHR}(\mathcal{I})), 1)], \quad (2)$$

where  $\text{CHR}$  is the application of CH-Rand augmentation, and  $H$  is the function of binary cross entropy to estimate the prediction error in classification. In implementation, we randomly sample a batch  $\mathcal{D}' \subseteq \mathcal{D}$  at each iteration to feed a half with augmentation and the other without.

### B. Anomaly Detection

For anomaly prediction, we use the feature representations  $g_\theta$  learnt within the classifier  $f_\Theta$  – i.e.,  $g_\theta$  is the output of an intermediate layer in  $f_\Theta$ . Whilst minimising the loss function in Equation (2), the representations of the normal training data  $\mathcal{D}$  are likely to be clustered to maximise the *distance* from anomalous data to effectively separate them. Therefore, similar to [29], we calculate the anomaly score  $s$  for an input image  $\mathcal{I}'$  by computing the average distance to the  $k$  nearest neighbors  $\mathcal{N} \subseteq \mathcal{D}$  in the space of  $g_\theta$ :  $s(\mathcal{I}') = (1/k) \sum_{\mathcal{I} \in \mathcal{N}} \delta(g_\theta(\mathcal{I}), g_\theta(\mathcal{I}'))$ , where  $\delta$  returns the Euclidean distance between two input vectors.

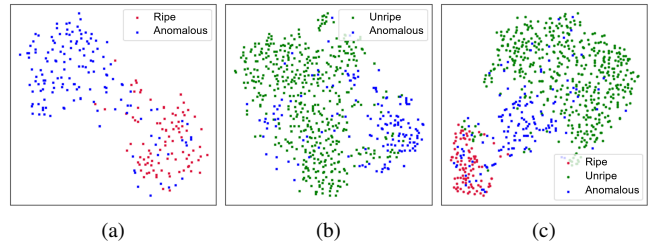


Fig. 3: t-SNE visualisations of learnt representations in CH-Rand on Riseholme-2021: (a) Ripe, (b) Unripe, and (c) Ripe&Unripe.

Our framework design is generic to easily replace this scoring module with other unsupervised techniques, such as Gaussian density estimators [30] or One-class SVM [31]. Yet, we use the  $k$ -neighbour heuristic since it has performed best in our tests.

## IV. EXPERIMENTS

We here offer the experimental results to demonstrate the performance of our proposed framework in vision-based monitoring of fruit anomalies. We first explain fruit anomaly detection datasets and technical details used through experiments in Section IV-A and Section IV-B, respectively. Section IV-C then shows quantitative results by comparison with other baselines, and based on the results, we examine in Section IV-D the relevance of the pretext task that CH-Rand generates to facilitate SL. Lastly, Section IV-E includes ablation studies to discuss variants of CH-Rand.

### A. Fruit Anomaly Detection Datasets

1) *Riseholme-2021*: For realistic evaluations, we first introduce Riseholme-2021, a new dataset of strawberry images, in which 3,520 images are available with manually annotated labels, such as Ripe, Unripe, Occluded, and Anomalous. This dataset was collected by deploying a commercial mobile robot *Thorvald* in the strawberry research farm at the Riseholme campus of the University of Lincoln as depicted in Fig. 1a. In particular, the robot was configured to use a side-mounted RGB camera to take images of normal and anomalous strawberries at various growth stages, whilst navigating along the lanes in polytunnels. Human experts then examined each image to manually crop the regions centered around strawberries and annotate with respective anomaly labels. In real applications, fruit segmentation algorithms could be employed to automate the extraction of fruit-centered regions, but in this work, we allow humans to intervene in the loop to minimise potential negative impacts caused by errors in segmentation process.

More specifically, each image from Ripe (Unripe) contains a single ripe (unripe) strawberry, whereas several ones may appear overlapping one another in images of the Occluded class. Furthermore, some strawberries in the Occluded class are observed to be covered by green stems. Anomalous cases also display single strawberries with



	All	Normal			Anomalous
		Ripe	Unripe	Occluded	
# of Images	3,520	462	2,406	499	153
Percentage	100.0%	13.1%	68.4%	14.2%	4.3%
Avg. W×H	63 × 66	75 × 81	59 × 61	71 × 75	60 × 60
Std. W×H	18 × 23	18 × 22	17 × 22	16 × 21	16 × 17

TABLE I: Statistics of Riseholme-2021. In this work, all subcategories except anomalous are included in normal class.

anomalies, such as the presence of malformations, the lack of normal pigmentation, or clear signals of disease. Example images of each category are displayed in Fig. 1b-1c.

Table I shows the basic statistics of the dataset, in which “normal” categories, including Ripe, Unripe, and Occluded have considerably more images (95.7%) than the Anomalous (4.3%) – i.e., this severe class imbalance provides a realistic testbed for anomaly detection. Riseholme-2021 is also presented with exclusive data sets – Train, Val, and Test – which contain 70%, 10%, and 20% “normal” images, respectively, and all Anomalous images are considered only during test. To further encourage active research in agri-technology, we publish our Riseholme-2021 dataset online at <https://github.com/ctyeong/Riseholme-2021>.

2) *Fresh & Stale*: Fresh & Stale<sup>1</sup> dataset contains annotated fruit images of six different species collected in controlled environments, and each image is labelled with either Fresh or Stale label. We, however, have discovered duplicate images that have been transformed with several methods – rotations or translations. We thus only keep images with unique contents, and as a result, the size of final dataset significantly is reduced, in which Apple is the largest class with 231 normal and 327 anomalous instances. Moreover, we only utilise Apple, Orange, and Banana since other classes each have less than 50 examples after the removal of duplicates. We set the split of normal data with Train (40%), Val (10%), and Test (50%) to conduct tests along with anomalous “stale” fruits. Also, the black pixels that the pre-transformation had produced were removed by conversion to white to match the original background.

### B. Implementation Details & Evaluation Protocols

Throughout experiments, we deploy a deep-network classifier for SL which consists of 5 ConvLayers followed by 2 DenseLayers, in which the number of  $3 \times 3$  convolutional filters incrementally increases (64, 128, 256, 512, and 512) as each layer is followed by a BatchNorm layer and a  $2 \times 2$  MaxPool layer, and the DenseLayers have 256 and 1 output nodes, respectively. Every layer uses LeakyReLU activations except the last layer with a sigmoid function. Note that though ResNet’s have shown successes in SL [32], we did not discover any benefit from using it (e.g., ResNet-18 as in [3]) possibly because of the small resolution of our images.

Also, at each training iteration, all inputs are resized to  $64 \times 64$  images and processed with traditional augmentations

<sup>1</sup><https://www.kaggle.com/raghavrpotdar/fresh-and-stale-images-of-fruits-and-vegetables>

before CH-Rand such as horizontal/vertical flips and color jitter<sup>2</sup>, which changes the brightness, contrast, saturation, and hue. Normalisations are also run to set pixel values bounded by  $[-1, 1]$  after all augmentations have been applied.

As in previous works for OC [1], [2], [3], the Area Under the Curve (AUC) of the Receiver Operating Characteristic (ROC) is used as the performance indicator, and the AUC of Precision-Recall (PR) curve is also reported as an additional metric considering the highly imbalanced class distribution in Riseholme-2021 (cf., Table I). Each AUC is the average of three individual runs to mitigate the random effects from CH-Rand and weight initialisations in networks.

In fact, other representation learning frameworks [3], [29] suggest a certain number of training iterations to achieve their best performance, although in practice, such knowledge is unavailable in advance. Our approach is, however, to regularly monitor the “validation accuracy” to stop training if the mean of the last five measurements reaches  $> .95$ , or 1.5K epochs have passed in order to deploy the model with the maximum validation accuracy. These criteria apply to all SL-based approaches in our experiments to evaluate the *relevance* of their pretext tasks to learn the final anomaly detection. More detail of the hyperparameter values with the code is available online at <https://github.com/ctyeong/CH-Rand>.

### C. Comparative Results

We compare CH-Rand with related methods mentioned in Section II – DCAE [1], DSVDD [2], IO-GEN [1], ROT [23], CP [3], and CH-Perm [26]. Note that for representation learning under SL, ROT and CP inject structural irregularities into images, while CH-Perm augments with randomly shuffled channels. A basic colour feature generator (HIST) is also considered, in which the number of pixels is counted within six unique ranges in each channel, and a representation of  $6 \times 6 \times 6$  dimensional colour histogram is produced per input combining the channel-wise ranges. Pretrained VGG16 [33] is also used to generate features to investigate the utility of the learnt features on ImageNet [8]. DOC [29] is also set up, which learns representations utilising an external benchmark dataset (e.g., CIFAR-10 [9])

Hyperparameter searches are conducted for each baseline to offer the best results on the Riseholme-2021 dataset first, albeit initial configurations are set up based on publicly available codes, e.g., DCAE’s performance dramatically improves with a smaller image size of  $32 \times 32$ . Since official source codes are not available for CP, we have implemented it based on the details on their appendix in [3]. In particular, we adopt the deep classifiers and the  $k$  neighbors-based detector described in Section III on ROT, CP, and CH-Perm so as to focus only on the achieved representation power in comparison to ours. The only distinction with ROT is to use four output nodes in the classifiers to predict four degrees of rotation – i.e.,  $0^\circ, 90^\circ, 180^\circ$ , and  $270^\circ$  – pre-applied to input images. Similarly, HIST and VGG16 run the

<sup>2</sup><https://pytorch.org/vision/stable/transforms.html>

Category	Metric	HIST	VGG16 [33]	DCAE [1]	DSVDD [2]	IOGEN [1]	DOC [29]	ROT [23]	CP [3]	CH-P ( $k=1$ ) [26]	CH-P ( $k=5$ ) [26]	CH-R ( $k=1$ ) (Ours)	CH-R ( $k=5$ ) (Ours)
Ripe	ROC	.915 $\pm .000$	.810 $\pm .000$	.874 $\pm .005$	.912 $\pm .006$	.887 $\pm .044$	.820 $\pm .000$	<b>.926</b> $\pm .003$	.911 $\pm .004$	.918 $\pm .005$	.922 $\pm .005$	.920 $\pm .004$	.922 $\pm .001$
	PR	.943 $\pm .000$	.864 $\pm .000$	.907 $\pm .003$	.935 $\pm .022$	.893 $\pm .057$	.883 $\pm .000$	<b>.958</b> $\pm .002$	.941 $\pm .006$	.949 $\pm .005$	.954 $\pm .004$	.955 $\pm .002$	.957 $\pm .001$
Unripe	ROC	.753 $\pm .000$	.621 $\pm .000$	.783 $\pm .003$	.810 $\pm .004$	.664 $\pm .046$	.698 $\pm .001$	.819 $\pm .007$	.860 $\pm .006$	.874 $\pm .012$	<b>.876</b> $\pm .012$	.873 $\pm .004$	.870 $\pm .006$
	PR	.556 $\pm .000$	.340 $\pm .000$	.486 $\pm .003$	.531 $\pm .010$	.342 $\pm .039$	.452 $\pm .000$	.554 $\pm .023$	.674 $\pm .028$	.709 $\pm .026$	.721 $\pm .026$	.755 $\pm .005$	<b>.765</b> $\pm .003$
Ripe & Unripe	ROC	.700 $\pm .000$	.623 $\pm .000$	.752 $\pm .002$	.727 $\pm .005$	.679 $\pm .023$	.642 $\pm .001$	.772 $\pm .009$	.780 $\pm .013$	.826 $\pm .004$	.829 $\pm .003$	.834 $\pm .008$	<b>.838</b> $\pm .007$
	PR	.385 $\pm .000$	.274 $\pm .000$	.426 $\pm .003$	.378 $\pm .012$	.334 $\pm .018$	.331 $\pm .000$	.428 $\pm .018$	.452 $\pm .026$	.572 $\pm .007$	.580 $\pm .008$	.607 $\pm .012$	<b>.615</b> $\pm .008$
All w/ Occluded	ROC	.673 $\pm .000$	.598 $\pm .000$	.715 $\pm .002$	.670 $\pm .012$	.609 $\pm .040$	.598 $\pm .001$	.736 $\pm .005$	.736 $\pm .007$	.795 $\pm .005$	.790 $\pm .005$	<b>.804</b> $\pm .014$	.796 $\pm .012$
	PR	.303 $\pm .000$	.228 $\pm .000$	.340 $\pm .003$	.295 $\pm .018$	.236 $\pm .026$	.252 $\pm .000$	.335 $\pm .016$	.337 $\pm .006$	.458 $\pm .016$	.436 $\pm .019$	<b>.496</b> $\pm .022$	.484 $\pm .021$

TABLE II: Average AUC-ROC scores on Riseholme-2021 with standard deviations from three independent runs for each model. HIST, VGG16, ROT, and CP also employ the  $k$  nearest neighbor detector with the best  $k \in \{1, 5, 10\}$ .

same detector to discern anomalies on their representations. In addition, the results obtained by the best  $k \in \{1, 5, 10\}$  are presented except CH-Rand and CH-Perm. Note here that all models including ours are then applied to Fresh & Stale without major modifications to assess the general capacity on variable conditions in agriculture. Lastly, CH-Rand uses representations  $g_\theta$  at `fc6` instead of `conv5`, and discussions on this design are described in Section IV-E.

1) *Riseholme-2021*: We test different combinations of normal classes against anomalies as shown in Table II. Every method struggles more with Unripe than Ripe and also with the cases where more normal types are involved since a larger variety of colours and shapes need to be modeled. In particular, the notable failure in DSVDD, HIST, IO-GEN, VGG16, and DOC indicates the challenge of the task with the strawberry images as all the wild conditions are concerned.

In overall, however, SL-based approaches, such as ROT, CP, CH-Perm, and CH-Rand, demonstrate more robust performance across categories despite their relatively simple designs of data augmentation and self-supervised learning. Still, significantly large drops of ROC are observed in ROT (.926  $\rightarrow$  .736) and CP (.911  $\rightarrow$  .736) compared to CH-Perm or CH-Rand (.922  $\rightarrow$  .790 in the worst model), as all normal subcategories are considered. Moreover, CH-Rand ( $k=1$ ) presents a 34% higher PR at least in Ripe&Unripe, and as Occluded class is also added, the margin increases up to 48%. This trend supports our motivation (cf., Section III-A) that representations of shapes could be little informative

Category	HIST	DCAE	ROT	CP	CH-P	CH-R
Apple	.873 $\pm .000$	.487 $\pm .008$	.718 $\pm .030$	.763 $\pm .021$	<b>.898</b> $\pm .011$	.892 $\pm .007$
Orange	.854 $\pm .000$	.554 $\pm .003$	.812 $\pm .010$	.816 $\pm .039$	.843 $\pm .010$	<b>.906</b> $\pm .004$
Banana	.856 $\pm .000$	.845 $\pm .017$	.973 $\pm .003$	.858 $\pm .013$	.975 $\pm .010$	<b>.992</b> $\pm .001$
All	.846 $\pm .000$	.648 $\pm .013$	.733 $\pm .016$	.827 $\pm .020$	.831 $\pm .010$	<b>.886</b> $\pm .016$

TABLE III: Average AUC-ROC scores on Fresh & Stale dataset. Successful approaches in Riseholme-2021 are compared using their best  $k \in \{1, 5, 10\}$  for  $k$ -neighbor detector.

for detection of fruit anomalies.

Table II also implies that though CH-Perm and CH-Rand are all trained for simply identifying unnatural colour patterns, their representations are not trivial features, because they significantly outperform HIST. CH-Rand provides slightly better results than CH-Perm in more complex normal sets probably because its higher randomness in augmentation simulates more realistic colour anomalies. Also, the hyperparameter  $k$  is not a dominating factor in the CH family.

For better understanding, Fig. 3 visualises representations in CH-Rand, in which the final features appear surprisingly useful for differentiation of anomalies though anomalous class was unavailable for explicit learning. In particular, Fig. 3c implies ambiguous appearances of anomalous samples to be represented between the ripe and unripe examples, so the final detector can take advantage of it.

2) *Fresh & Stale*: Table III shows that DCAE is not as effective as in Riseholme-2021 with highly varying ROC's in different categories, i.e. .487  $\sim$  .845, since it easily overfits the less complex images with controlled backgrounds.

Interestingly, HIST works significantly better here than in Riseholme-2021 even outperforming ROT and CP probably taking advantage of homogeneous colour patterns in focal objects, and consequently, anomalous visual signals such as black spots on bananas are easily differentiated simply by colour frequencies. The failure of the two SL methods re-emphasises the lesser importance of local structural features in fruit anomaly identification.

Also, CH-Perm particularly struggles with Orange and All, in which it loses to HIST. CH-Rand, however, presents consistently high performance across all fruit species.

#### D. Relevance of SL task

Table IV reveals the correlations between the validation accuracies during SL and the ROC's finally achieved to examine relevance of each pretext task to the fruit anomaly detection. CH-Rand leads to a positively correlated task in all datasets, while others have negative coefficients in Fresh & Stale. That is, successful pre-task training with CH-Rand can better ensure representations for building precise

Dataset	ROT	CP	CH-P	CH-R
Riseholme-2021	+199	+290	+811	+739
Fresh & Stale	-.554	-.529	-.244	+275

TABLE IV: Pearson correlation coefficients between AUC-ROC scores and validation accuracies measured during SL proxy tasks. “All” categories are considered for each dataset.

	Patch	Sobel	Th.25	Th.50	Th.75	Sp.75	All
ROC	.674	.731	.696	.716	.742	.725	<b>.749</b>

TABLE V: Performance of CH-Rand on Riseholme-2021 depending on the selection of pixels.

	CH-S	CH-P				CH-R			
	32	32	64	64 $\text{fc6}$	96	32	64	64 $\text{fc6}$	96
ROC	.710	.755	.773	.769	.753	.749	.779	<b>.781</b>	.775

TABLE VI: Performance of CH-Split, CH-Perm, and CH-Rand on Riseholme-2021 with different input sizes. Utilising representations learnt at  $\text{fc6}$  layer is also considered.

fruit anomaly detector, but continued training with other augmentations may rather *degrade* the performance of final fruit detector particularly on Fresh & Stale data. With CH-Rand, we hence suggest using the validation accuracy as a practical metric for early stopping, while other previous frameworks manually searched for optimal numbers of iterations as another hyperparameter [3], [29].

### E. Ablation Study

We here investigate the effects of various randomisation methods and hyperparameters that define our augmentation techniques. To save computation time, we train models only on a half of training set of all normal classes in Riseholme-2021. Also, each image is resized to  $32 \times 32$ , and the utilised representations of  $g_\theta$  are always extracted at  $\text{conv5}$  layer unless mentioned otherwise to focus on each parameter in order. Moreover,  $k$  is set to 1 to only consider the nearest neighbor from training data to calculate the anomaly score.

1) *Pixel Selection*: Although CH-Rand is proposed to apply randomised channels across all pixels in the entire image, we here explore the effects of applications to local regions in  $n$ -pixel images. The tested methods are below, and Fig. 2 displays some examples:

- *Patch*: Pixels inside a random rectangular patch [3]
- *Sobel*: Pixels inside a large segmented region from Sobel filter-based segmentation [28].
- *Th $\Delta$* : Pixels thresholded between rank  $r$  and  $r + \lceil n \times \Delta \rceil$  in grayscale image, where  $r \sim \mathcal{U}(1, n - \lceil n \times \Delta \rceil)^3$ .
- *SP $\Delta$* : Randomly sampled sparse  $\lceil n \times \Delta \rceil$  pixels.
- *All*: All pixels as proposed in Section III-A.

In Table V, we discover that CH-Rand works poorly when objectness is not taken into account. To be specific, Patch, which may position a patch lying across multiple semantic objects, leads to the worst results. Similarly, when 75% pixels

<sup>3</sup>Discrete uniform distribution

are sparsely augmented with SP.75, the performance is worse than Th.75, which tends to pick pixels around the same part of objects as a result of thresholding. The high performance of Sobel also supports this idea.

Another key observation is that CH-Rand on more pixels produces better results. For instance, Th. $\Delta$  presents the improvements as  $\Delta$  increases, and finally when *all pixels* are involved as designed in Section III-A, the highest ROC is achieved. Thus, all pixels are considered hereafter.

2) *Randomisation Variants & Input Size*: We also explore various randomisation methods in different sizes of images:

- *CH-Split*: Channel Splitting, which copies a randomly chosen channel to others [27].
- *CH-Perm*: Channel Permutation, which uses a random permutation of channels without repetition [26].
- *CH-Rand*: Channel Randomisation in Section III-A.

In Table VI, CH-Split leads to the lowest performance implying that its three possible outputs – i.e., RRR, GGG, BBB – only provide limited irregular patterns to learn compared to other randomisations. CH-Perm and CH-Rand all appear to work best with  $64 \times 64$  images probably because the average size of the dataset is  $63 \times 66$  (cf., Table I). With that optimal size, CH-Rand slightly outperforms CH-Perm.

3) *Layer Selection*: In Table VI, more improvement is also discovered in CH-Rand with representations at  $\text{fc6}$  implying that the most discriminative representations are learnt there to offer the best features to the last  $\text{fc7}$  layer. Note that we have consistently observed such a tendency with CH-Rand, though CH-Perm did not take any benefit.

Thus, based on all these findings, the best configuration for each model has been adopted in Section III and Section IV.

## V. CONCLUSIONS & FUTURE WORK

We have proposed a novel data augmentation method for self-supervised representation learning to effectively identify fruit anomalies in agri-robotic applications. Our CH-Rand method has demonstrated consistently reliable capability on all tested types of fruit in various conditions compared to other baselines. In particular, all experimental results have supported our hypothesis that learning irregularities in colour is more useful than learning of atypical structural patterns for building precise fruit anomaly detectors.

In addition, we have suggested monitoring validation accuracy for early stopping during training because our statistical analysis has indicated positive correlations between the success in the pretext task of CH-Rand and the performance of finally built anomaly detector. For realistic scenarios, we also have introduced a new image dataset, so-called *Riseholme-2021*, in which over 3.5K strawberry images at various growth stages are contained along with anomalous examples.

In future work, we could consider additional modalities of sensory data such as texture to improve overall detection performance. We could also acquire an extended dataset to include more maturity stages including flowers and apply the method to detection of diseases affecting plant leaves. Furthermore, more fine-grained detection could be developed to automatically identify local anomalies.



## REFERENCES

- [1] T. Choi, B. Pyenson, J. Liebig, and T. P. Pavlic, "Identification of abnormal states in videos of ants undergoing social phase change," in *Proceedings of the AAAI Conference on Artificial Intelligence*, vol. 35, no. 17, 2021, pp. 15 286–15 292.
- [2] L. Ruff, R. Vandermeulen, N. Goernitz, L. Deecke, S. A. Siddiqui, A. Binder, E. Müller, and M. Kloft, "Deep one-class classification," in *International conference on machine learning*. PMLR, 2018, pp. 4393–4402.
- [3] C.-L. Li, K. Sohn, J. Yoon, and T. Pfister, "CutPaste: Self-supervised learning for anomaly detection and localization," in *Proceedings of the IEEE/CVF Conference on Computer Vision and Pattern Recognition*, 2021, pp. 9664–9674.
- [4] T. DeVries and G. W. Taylor, "Improved regularization of convolutional neural networks with cutout," *arXiv preprint arXiv:1708.04552*, 2017.
- [5] J. Yi and S. Yoon, "Patch SVDD: Patch-level SVDD for anomaly detection and segmentation," in *Proceedings of the Asian Conference on Computer Vision*, 2020.
- [6] D. Hendrycks, M. Mazeika, S. Kadavath, and D. Song, "Using self-supervised learning can improve model robustness and uncertainty," *Advances in Neural Information Processing Systems*, vol. 32, pp. 15 663–15 674, 2019.
- [7] P. Bergmann, K. Batzner, M. Fauser, D. Sattlegger, and C. Steger, "The MVTEC anomaly detection dataset: a comprehensive real-world dataset for unsupervised anomaly detection," *International Journal of Computer Vision*, vol. 129, no. 4, pp. 1038–1059, 2021.
- [8] J. Deng, W. Dong, R. Socher, L.-J. Li, K. Li, and L. Fei-Fei, "Imagenet: A large-scale hierarchical image database," in *2009 IEEE conference on computer vision and pattern recognition*. Ieee, 2009, pp. 248–255.
- [9] A. Krizhevsky, G. Hinton *et al.*, "Learning multiple layers of features from tiny images," 2009.
- [10] B. Espejo-Garcia, N. Mylonas, L. Athanasakos, E. Vali, and S. Fountas, "Combining generative adversarial networks and agricultural transfer learning for weeds identification," *Biosystems Engineering*, vol. 204, pp. 79–89, 2021.
- [11] X. Wu, S. Aravecchia, P. Lottes, C. Stachniss, and C. Pradalier, "Robotic weed control using automated weed and crop classification," *Journal of Field Robotics*, vol. 37, no. 2, pp. 322–340, 2020.
- [12] P. Bosilj, E. Aptoula, T. Duckett, and G. Cielniak, "Transfer learning between crop types for semantic segmentation of crops versus weeds in precision agriculture," *Journal of Field Robotics*, vol. 37, no. 1, pp. 7–19, 2020.
- [13] S. Mghames, M. Hanheide, and A. Ghalamzan, "Interactive movement primitives: Planning to push occluding pieces for fruit picking," in *2020 IEEE/RSJ International Conference on Intelligent Robots and Systems (IROS)*. IEEE, 2020, pp. 2616–2623.
- [14] Y. Ge, Y. Xiong, and P. J. From, "Classification of pickable and unpickable strawberries under farm conditions," in *2020 IEEE 16th International Conference on Automation Science and Engineering (CASE)*. IEEE, 2020, pp. 961–966.
- [15] K. P. Ferentinos, "Deep learning models for plant disease detection and diagnosis," *Computers and Electronics in Agriculture*, vol. 145, pp. 311–318, 2018.
- [16] U. P. Singh, S. S. Chouhan, S. Jain, and S. Jain, "Multilayer
- [17] J. Gao, J. C. Westergaard, E. H. R. Sundmark, M. Bagge, E. Liljeroth, and E. Alexandersson, "Automatic late blight lesion recognition and severity quantification based on field imagery of diverse potato genotypes by deep learning," *Knowledge-Based Systems*, vol. 214, p. 106723, 2021.
- convolution neural network for the classification of mango leaves infected by anthracnose disease," *IEEE Access*, vol. 7, pp. 43 721–43 729, 2019.
- [18] E. Hossain, M. F. Hossain, and M. A. Rahaman, "A color and texture based approach for the detection and classification of plant leaf disease using knn classifier," in *2019 International Conference on Electrical, Computer and Communication Engineering (ECCE)*. IEEE, 2019, pp. 1–6.
- [19] H. R. Kerner, D. F. Wellington, K. L. Wagstaff, J. F. Bell, C. Kwan, and H. B. Amor, "Novelty detection for multi-spectral images with application to planetary exploration," in *Proceedings of the AAAI Conference on Artificial Intelligence*, vol. 33, no. 01, 2019, pp. 9484–9491.
- [20] M. Sabokrou, M. Khalooei, M. Fathy, and E. Adeli, "Adversarially learned one-class classifier for novelty detection," in *Proceedings of the IEEE Conference on Computer Vision and Pattern Recognition*, 2018, pp. 3379–3388.
- [21] T. Schlegl, P. Seeböck, S. M. Waldstein, G. Langs, and U. Schmidt-Erfurth, "f-anogan: Fast unsupervised anomaly detection with generative adversarial networks," *Medical image analysis*, vol. 54, pp. 30–44, 2019.
- [22] P. Perera, R. Nallapati, and B. Xiang, "Ocgan: One-class novelty detection using gans with constrained latent representations," in *Proceedings of the IEEE/CVF Conference on Computer Vision and Pattern Recognition*, 2019, pp. 2898–2906.
- [23] S. Gidaris, P. Singh, and N. Komodakis, "Unsupervised representation learning by predicting image rotations," in *International Conference on Learning Representations*, 2018.
- [24] C. Vondrick, A. Shrivastava, A. Fathi, S. Guadarrama, and K. Murphy, "Tracking emerges by colorizing videos," in *Proceedings of the European conference on computer vision (ECCV)*, 2018, pp. 391–408.
- [25] G. Larsson, M. Maire, and G. Shakhnarovich, "Colorization as a proxy task for visual understanding," in *Proceedings of the IEEE Conference on Computer Vision and Pattern Recognition*, 2017, pp. 6874–6883.
- [26] H. Lee, S. J. Hwang, and J. Shin, "Self-supervised label augmentation via input transformations," in *International Conference on Machine Learning*. PMLR, 2020, pp. 5714–5724.
- [27] H.-Y. Lee, J.-B. Huang, M. Singh, and M.-H. Yang, "Unsupervised representation learning by sorting sequences," in *Proceedings of the IEEE International Conference on Computer Vision*, 2017, pp. 667–676.
- [28] scikit image, "Image Segmentation," [https://scikit-image.org/docs/dev/user\\_guide/tutorial\\_segmentation.html](https://scikit-image.org/docs/dev/user_guide/tutorial_segmentation.html).
- [29] P. Perera and V. M. Patel, "Learning deep features for one-class classification," *IEEE Transactions on Image Processing*, vol. 28, no. 11, pp. 5450–5463, 2019.
- [30] O. Rippel, P. Mertens, and D. Merhof, "Modeling the distribution of normal data in pre-trained deep features for anomaly detection," in *2020 25th International Conference on Pattern Recognition (ICPR)*. IEEE, 2021, pp. 6726–6733.
- [31] B. Schölkopf, J. C. Platt, J. Shawe-Taylor, A. J. Smola, and R. C. Williamson, "Estimating the support of a high-dimensional distribution," *Neural computation*, vol. 13, no. 7, pp. 1443–1471, 2001.
- [32] A. Kolesnikov, X. Zhai, and L. Beyer, "Revisiting self-supervised visual representation learning," in *Proceedings of the IEEE/CVF conference on computer vision and pattern recognition*, 2019, pp. 1920–1929.
- [33] K. Simonyan and A. Zisserman, "Very deep convolutional networks for large-scale image recognition," in *International Conference on Learning Representations*, 2015.